

Characterization of FePd bilayers and trilayers using soft x-ray resonant magnetic scattering and micromagnetic modeling

G. Beutier,¹ G. van der Laan,² K. Chesnel,^{1,3} A. Marty,¹ M. Belakhovsky,¹ S. P. Collins,^{2,4} E. Dudzik,^{2,5} J.-C. Toussaint,⁶ and B. Gilles⁷

¹*DRFMC, CEA-Grenoble, 17 Avenue des Martyrs, 38054 Grenoble, France*

²*Magnetic Spectroscopy, Daresbury Laboratory, Warrington, WA4 4AD, United Kingdom*

³*ALS, Lawrence Berkeley National Laboratory, 1 Cyclotron Road, Berkeley, California 94720, USA*

⁴*Diamond Light Source, Rutherford Appleton Laboratory, Didcot OX11 0QX, United Kingdom*

⁵*Hahn-Meitner-Institut/Bessy, Albert-Einstein Strasse, D-12489 Berlin, Germany*

⁶*Laboratory Louis Néel, CNRS, Boîte Postale 166, Grenoble Cedex 9, France*

⁷*LTPCM, INPG, Boîte Postale 75, 38402 Saint Martin d'Hères Cedex, France*

(Received 5 November 2004; revised manuscript received 15 February 2005; published 31 May 2005)

We have studied bilayers and trilayers of FePd thin-film alloys, where each of the constituting layers has a different magnetic anisotropy, as controlled by the growth conditions. The competition between the magneto-crystalline anisotropy and the shape anisotropy in these films leads to the formation of stripe domains with a period of ~ 100 nm, which has been imaged by magnetic force microscopy (MFM). The average magnetic anisotropy has been obtained from the in-plane and perpendicular magnetic field dependence, measured using vibrating sample magnetometry (VSM). We measured the soft x-ray resonant magnetic scattering (SXRMS) at the Fe L_3 edge using σ linearly polarized light, which is sensitive to the magnetization profile in the layers. The magnetic configuration of the layer systems was modeled using micromagnetic software (GL-FFT, ©CNRS). The results of the micromagnetic modeling were used for a numerical simulation of the reflectivity scan and the magnetic rod scans of the SXRMS. This allowed us to determine parameters, such as the lateral roughness, the magnetic period, the magnetic correlation length, and the magnetic layer thickness. The good agreement obtained with the experimental results demonstrates that SXRMS provides in-depth information that cannot be obtained from either MFM or VSM.

DOI: 10.1103/PhysRevB.71.184436

PACS number(s): 75.75.+a, 75.25.+z, 78.70.Ck, 75.50.Bb

I. INTRODUCTION

Recent developments in magnetic data storage have resulted in a strong interest for ferromagnetic materials displaying perpendicular magnetic anisotropy. Among the most promising systems are alloys exhibiting the $L1_0$ structure, such as FePt, CoPt, and FePd, displaying periodic stripe formations of alternating up and down domains.¹ Several methods are available to characterize the magnetic properties of thin films. Among these, magneto-optical methods are most prominent and have the advantage that they can be performed under applied magnetic and electric fields. However, magneto-optics in the visible region lacks element specificity and moreover the ultimate spatial resolution is limited by the wavelength. The discovery of strong magneto-optical effects in the core level x-ray absorption edges of magnetic elements² has opened up new possibilities, such as the separation of the spin and orbital part of the magnetic moments³ and the determination of the magnetic anisotropy.⁴ Such techniques strongly benefit from the advent of undulator devices offering variable linear and circular polarization of the intense synchrotron radiation.

Scattering experiments have so far mainly been restricted to the region of the hard x rays, offering high spatial resolution and large penetration. However, in the soft x-ray range the resonant magnetic scattering cross sections are much stronger and although the soft x-ray wavelength is normally too long to determine the unit cell structure, its length scale

matches perfectly to the nanoscopic structure of domains and artificially structured devices. Soft x-ray resonant magnetic scattering (SXRMS) has the ability to cover the length scale from 1 to 1000 nm and is relatively easy to perform on *ex situ* prepared samples.^{5,6} Element specificity and magnetic sensitivity are obtained by tuning the x-ray energy to the appropriate absorption edge. For $3d$ transition metals, the excitation of $2p$ electrons into unoccupied $3d$ states leads to strong absorption edges with energies in the soft x-ray region.⁷ Applications of SXRMS include the characterization of structural and magnetic properties of layered and domain systems especially their interface roughness, induced magnetic order in nonmagnetic spacer layer, layer-resolved magnetic moments, and local magnetic configuration using coherent radiation.⁸⁻²¹

FePd thin films can be grown with varying degrees of perpendicular magnetic anisotropy (PMA) by codepositing Fe and Pd at elevated temperatures. Depending on the precise growth conditions, the alloy layers are more or less chemically ordered, with Fe and Pd occupying alternating layers in a tetragonally distorted face-centered-cubic phase $L1_0$. This chemical ordering leads to the PMA, so that the anisotropy increases with the degree of order.²² The competition between the PMA and the thin-film shape anisotropy leads to domains with up and down magnetization perpendicular to the film plane. The formation of magnetic closure domains will reduce the energy of the magnetic flux lines outside the sample. Dürr *et al.*⁸ demonstrated the presence of

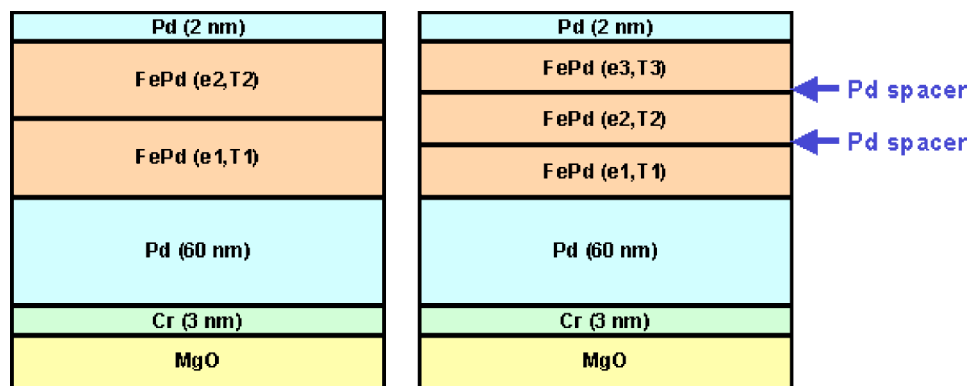


FIG. 1. (Color online) Schematic diagrams of the multiple layer systems. Left-hand side: bilayer; right-hand side: trilayer. The different thicknesses and growth temperatures are denoted by e_i and T_i , respectively.

these closure domains using SXRMS at the Fe L_3 absorption edge with circularly polarized x rays. Dudzik *et al.*^{23,24} studied the influence of PMA on closure domains in FePd films using SXRMS by fitting the circular dichroism in the magnetic scattering in combination with the structure in the magnetic rod scans. Closure domains with in-plane magnetization become energetically unfavorable in samples with strong PMA because of the preference for the easy-axis to be perpendicular to the surface.

In this paper we present a study of FePd bilayer and trilayer samples, where each layer has a different magnetic anisotropy due to growth conditions. Comparative studies on a single homogeneous FePd layer were already presented in Ref. 25. We use various techniques, such as magnetic force microscopy (MFM), vibrating sample magnetometry (VSM), micromagnetic modeling, and SXRMS. The stripe pattern can be observed using MFM imaging. MFM probes the magnetic stray fields and the images reveal the magnetization in the perpendicular direction. The technique of VSM gives the average information about the magnetization. SXRMS gives access to information which is complementary to MFM and VSM, such as the closure domains, the (magnetic) depth profile, and the (magnetic) correlation length. In order to analyze the SXRMS results, we use the micromagnetic simulation of the magnetic configuration of the layer system calculated with the Gilbert-Landau-Lifshitz method. The modeled magnetic configuration is used to calculate the reflectivity and the magnetic rod scans using the formalism for SXRMS. The results allow one to reiterate some of the parameters in the micromagnetic simulations. Some preliminary results have been published elsewhere.²⁶

The outline of this paper is as follows. Section II describes the thin-film preparation, which tailors the magnetic anisotropy. Section III describes the characterization of the magnetic anisotropy of the bilayer and trilayer systems using MFM imaging and VSM measurements. Section IV gives some experimental details of the SXRMS technique and presents the measured results of the reflectivity and magnetic rod scans. Section V outlines the theoretical background of the micromagnetic simulations and gives the results of the numerical modeling for the different systems. Section VI describes the numerical simulation of the SXRMS measurements for the magnetic configurations obtained by the micromagnetic numerical modeling. It is also shown what kind of information can be obtained. Finally, conclusions are drawn in Section VII.

II. SAMPLE PREPARATION

The systems of interest are self-organizing magnetic patterns as formed in thin films of FePd alloys,¹ where the magnetization breaks up in domains of different directions in order to reduce the stray field energy.²⁷ The samples were grown at the Commissariat à l’Energie Atomique (CEA) in Grenoble, by molecular beam epitaxy (MBE), on MgO(001) substrates. Growth conditions were varied to obtain a range of different anisotropies. The perpendicular magnetic anisotropy can be quantified by the quality factor $Q = K_u / 2\pi M_s^2$, where K_u is the perpendicular anisotropy constant and M_s is the saturation magnetization per volume unit. The magnetic configuration depends on both the layer thickness and the Q , which strongly depends on the disorder as controlled by the deposition temperature.^{22,28} We can distinguish between weak anisotropy ($Q < 1$), where the magnetization gradually rotates over the domain walls, forming closure domains, and strong anisotropy ($Q > 1$) that gives rise to the interlaced domains with smaller wall thickness.²⁵

We have grown successive FePd layers with different anisotropies and thicknesses on top of each other (cf. the schematic diagrams in Fig. 1) in order to study their magnetic interactions. We select the mode of codeposition, for which the degree of anisotropy is controlled by the deposition temperature. Room temperature gives $Q \approx 0$, while an elevated temperature of 400 °C gives $Q \approx 1.8$. However, the specific values of Q for each of the layers cannot be measured. Once the deposition is completed, the VSM measurements in the perpendicular and parallel geometry can only give the average anisotropy Q_{av} of the entire sample.

The different bilayers and trilayers that were characterized and studied are shown in Table I. The thickness of each individual layer is 10, 20, or 30 nm. The six bilayers can be divided into two groups according to their deposition order. A first group includes the bilayers B1, B2, B3, and B4, grown by first depositing, at ambient temperature, the disordered FePd layer with quasi-zero anisotropy, then subsequently, at elevated temperature, the ordered layer with strong anisotropy. The bilayers B5 and B6, forming the second group, were grown in reversed order.

The trilayers correspond to a kind of “magnetic sandwich” where the central layer with strong anisotropy is enclosed between two disordered layers of 10 nm thickness. The central layer has a thickness of 20 nm (T1 and T3) or 10 nm (T2 and T4). Moreover, in the samples T3 and T4,

TABLE I. Description of the studied FePd bilayers and trilayers, with nominal thicknesses e_i (nm) and growth temperatures T_i ($^{\circ}\text{C}$) for each layer i and the total thickness e_{tot} . (See Fig. 1 for the layer index i .)

Sample	T_1	e_1	Spacer	T_2	e_2	Spacer	T_3	e_3	e_{tot}
B1	20	30		400	30				60
B2	20	10		400	30				40
B3	20	10		400	10				20
B4	20	30		400	10				40
B5	400	30		0	10				40
B6	400	30		0	30				60
T1	20	10		400	20		20	10	40
T2	20	10		400	10		20	10	30
T3	20	10	2	400	20	2	20	10	44
T4	20	10	2	400	10	2	20	10	34

nonmagnetic Pd spacer layers of 2 nm thickness were deposited at the position of the magnetic interfaces. The thickness of the spacer layers was 2 nm, which is within the limit of the exchange coupling between the magnetic FePd layers.

III. MAGNETIC CHARACTERIZATION

A. MFM

MFM gives access to the stray fields and hence allows us to image the magnetic domains. The MFM images of the samples as deposited are reproduced in Fig. 2. All samples exhibit domains of perpendicular magnetization, except B4. In this sample the layer with strong anisotropy is indeed too thin (10 nm) compared to the soft layer (30 nm), which imposes an in-plane magnetization up to the surface. Therefore the exchange coupling dominates over the anisotropy and prevents the formation of perpendicularly magnetized domains.

The samples B1, B2, and B3, with a layer of strong anisotropy grown on top of a soft layer, exhibit well-aligned stripes, whereas samples B5 and B6, grown in reversed order, show interlaced domains. The latter is due to the in-plane magnetization of the soft layer, which influences the formation of domains in the anisotropic layer during its growth, whereas the domains form without any restraint when the anisotropic layer is grown first. This is an effect of the dipole coupling between both layers, which is strong enough to align domains during their nucleation but not once they are already formed. The MFM image of the bilayer B6 shows less contrast than that of B5, because the disordered layer is thicker, so that the in-plane magnetization component is reinforced at the cost of the perpendicular component, thereby diminishing the stray fields.

Looking at the images of the trilayers, the samples T1 and T2 exhibit aligned stripes, while T3 and T4 show interlaced domains. This is another consequence of the dipolar coupling of the layers. In T1 and T2 the domains are influenced during their nucleation by the in-plane magnetization of the underlying layer, whereas in T3 and T4 the Pd spacers reduce the

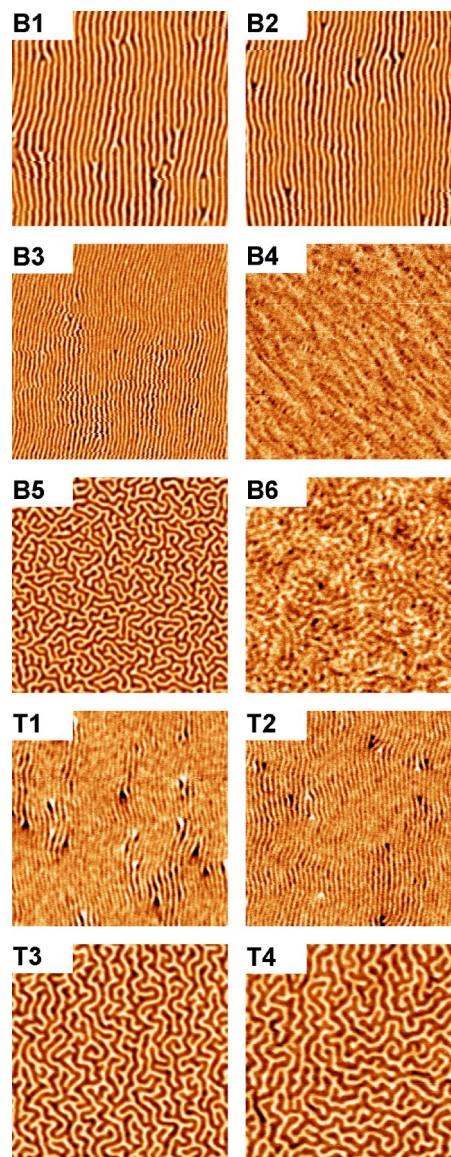


FIG. 2. (Color online) MFM images of the samples, measured “as deposited.” The image size is $4\ \mu\text{m} \times 4\ \mu\text{m}$.

strength of the coupling. Furthermore, the number of forks is higher for sample T1 than for T2 because of the larger thickness of the ordered layer, i.e., the effect of the magnetic anisotropy, is more important.

The average period of the magnetic stripes, deduced from the MFM images, varies from 85 to 200 nm, as listed in Table II. This magnetic period decreases strongly with the total FePd thickness, going from a period of 133 to 85 nm when the total thickness changes from 60 to 20 nm. This trend is in agreement with the theoretical prediction developed by Kaplan and Gehring.^{29,30} The width of the interlaced domains also increases with thickness and they are also wider than the stripe domains for samples with comparable thickness.

B. VSM

VSM has been performed in both parallel and perpendicular geometry (Fig. 3) in order to obtain information about the

TABLE II. Magnetic characteristics of the studied FePd bilayers and trilayers. The magnetic stripe period p_{mag} (nm) evaluated from the MFM image, the average quality factor Q_{av} (nm) (within 10%) obtained from VSM measurements, and the theoretical quality factor Q_{th} (nm) [see Eq. (2)].

Sample	MFM	p_{mag} (MFM)	Q_{av} (VSM)	Q_{th}
B1	Parallel stripes	133	0.95	0.80
B2	Parallel stripes	107	1.35	1.20
B3	Parallel stripes	85	0.86	0.8
B4	No domains		~ 0.2	0.4
B5	Interlaced serpentes	133	1.25	1.20
B6	Interlaced serpentes	150	0.65	0.80
T1	Parallel stripes	105	0.9	0.8
T2	Parallel stripes	92	0.7	0.53
T3	Interlaced domains	172	1	0.8
T4	Interlaced domains	192	0.6	0.53

global magnetization of the samples. In the parallel geometry, the curves exhibit a magnetization step around zero field, due to the very low coercivity of the FePd soft layers which follows the field direction. The step height corresponds to the total amount of in-plane magnetization in the sample and agrees well with the relative amount of FePd soft layer as obtained from the thicknesses. The bilayer B4 is saturated in-plane by a quasi-zero magnetic field, which confirms that the sample magnetization is nearly completely in-plane and which explains the absence of magnetic domains in the MFM image.

The measurements under perpendicular field exhibit a kink (except for B4) corresponding to the saturation of the hard layer, which is easier to saturate than the soft layers. As expected, samples with a thicker anisotropy layer and a thinner soft layer are easier to saturate. In the trilayers, the saturation of the anisotropic layer is achieved at lower field for a sample with Pd spacers between the magnetic layers compared to an equivalent sample without Pd spacers. This shows that the 2 nm thick spacer layers decouple the FePd layers.

The difference between the in-plane and perpendicular magnetization curves allows one to evaluate an average anisotropy constant Q_{av} for the entire sample. In a simple model we can write the magnetic energy per unit volume in the sample as the sum over the different contributions for the dipolar term, the magnetic anisotropy term, and the Zeeman term,

$$E_{\text{mag}} = 2\pi M_s^2 \cos^2 \alpha + K_u \sin^2 \alpha - HM_s \cos \beta, \quad (1)$$

where α is the angle between magnetization and surface normal and β is the angle between magnetization and applied field. The energy difference between the two saturated states ($\alpha=0^\circ$ and 90° with $\beta=0^\circ$) is $\Delta E_{\text{sat}} = K_u - 2\pi M_s^2$.

The energy required to make a small change in the magnetic state is HdM , so that the energy difference between the nonmagnetized state and the saturated state is $\int_0^{M_s} HdM$. Therefore the energy difference between the two saturated

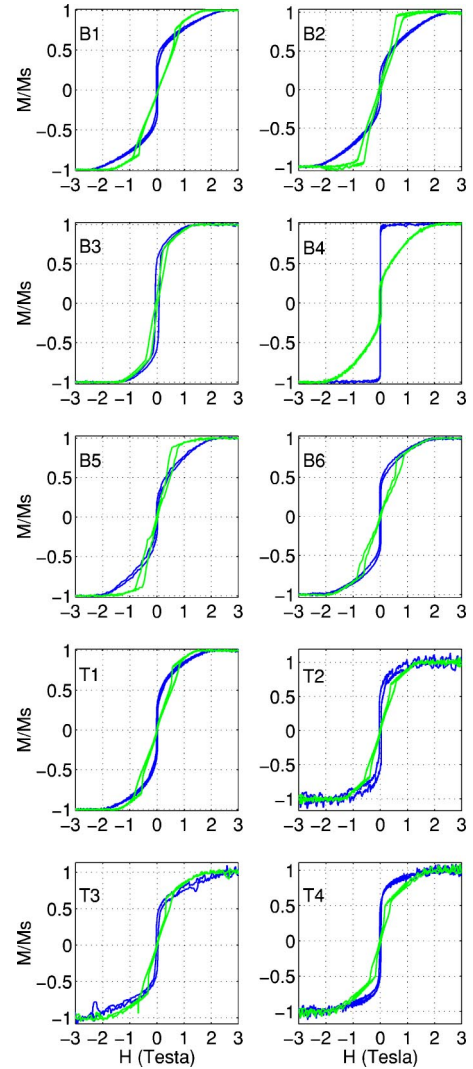


FIG. 3. (Color online) VSM measurements of the magnetization cycles in parallel (dark gray or blue curve) and perpendicular (light gray or green curve) magnetic field. The magnetization is normalized to the saturation magnetization M_s .

states is $\Delta E_{\text{sat}} = \int_0^{M_s} (H_{\perp} - H_{\parallel}) dM$, which is the area between both magnetization curves (Fig. 4). From this we deduce K_u and therefore $Q_{\text{av}} = K_u / 2\pi M_s^2$ since we know M_s .

Since K_u is an energy per unit volume, we can evaluate a “theoretical” global value for the sample from the layer thicknesses according to $K_{\text{th}} = (\sum_i e_i K_i) / (\sum_i e_i)$, where e_i is the thickness of the layer i . Assuming the magnetization is the same for each layer, we can write

$$Q_{\text{th}} = \frac{\sum_i e_i Q_i}{\sum_i e_i}. \quad (2)$$

The numerical values were calculated assuming $Q_i = 1.8$ in FePd layers grown at elevated temperatures and $Q_i = 0$ in FePd layers grown at room temperature. Table II compares the values of the quality factor Q_{av} , deduced from the VSM measurements, with the theoretical values Q_{th} , calculated using Eq. (2). The measured Q_{av} is in relatively good agree-

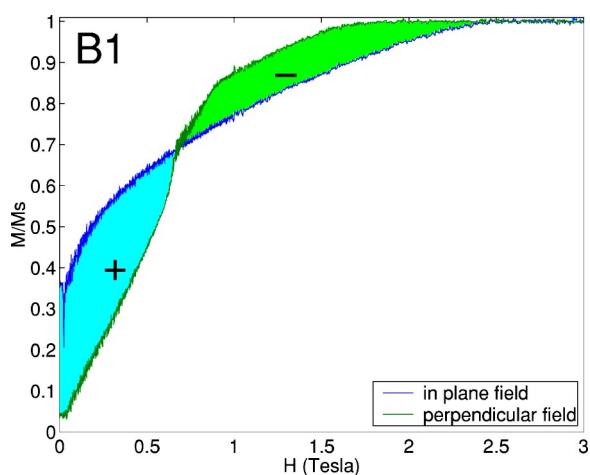


FIG. 4. (Color online) Comparison of the magnetization curves in parallel (dark gray or blue curve) and perpendicular (light gray or green curve) magnetic fields for the sample B1.

ment with the estimated Q_{th} . The small differences can be ascribed to several origins, in particular, a temperature change during the fabrication can generate diffusion phenomena, modifying the chemical structure at the interfaces and consequently changing the degree of anisotropy.

IV. SXRMS

While MFM gives access to the stray fields and VSM measurements show the global anisotropic magnetic behavior of the sample, SXRMS allows the study of the in-depth magnetic profile. The absorption length, l_{abs} , of x rays tuned to the Fe L_3 edge in FePd alloy is ~ 30 nm, which is sufficient to study the magnetic profile in our samples, whose total FePd thickness is below $2l_{abs}$. The coupling between layers of different anisotropy should show up in the magnetic profile as a rather sharp transition between in-plane and perpendicular magnetization and gives a propagation of the magnetic periodicity into the soft layer.

The magnetic scattering experiments were carried out in a two-circle diffractometer using polarized x rays from beamline 1.1 of the Synchrotron Radiation Source (SRS) at Daresbury Laboratory (UK). Details of the θ - 2θ in-vacuum diffractometer can be found elsewhere.^{5,6,31} All experimental results presented and simulated here were obtained with the samples mounted in the transverse geometry, i.e., with the scattering plane (x,z) perpendicular to the stripe direction (y). Figure 5 shows the schematics of the experimental geometry. The light was tuned to the Fe L_3 edge ($E = 709$ eV, $\lambda = 1.75$ nm) and σ polarized, i.e., linearly polarized perpendicular to the scattering plane, hence probing the electronic density through the $\sigma \rightarrow \sigma$ polarization channel and the magnetization through the $\sigma \rightarrow \pi'$ polarization channel. Given the geometrical factor in the magnetic scattering [Eq. (10)], only the component of the magnetization parallel to the outgoing beam, which is in the xz plane, is probed. Three different types of measurements were performed on

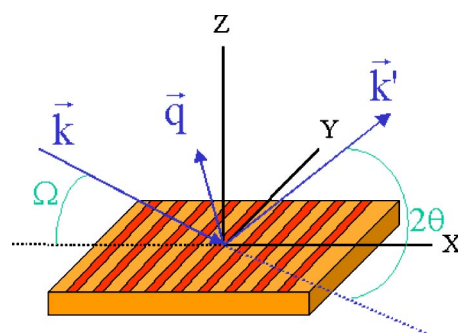


FIG. 5. (Color online) Schematics of the transverse geometry used in the scattering measurement.

each sample, namely reflectivity measurements, transverse scans, and truncation rods.

Resonant reflectivity measurements probe the laterally averaged electronic and magnetic depth profile. In our samples, only the y component of the magnetization, which is not probed in the transverse geometry with σ -polarized light, has a nonzero constant part. Therefore no magnetic effect was observed in the resonant reflectivity measurements, and the contrast between off-resonance and on-resonance can be ascribed to nonmagnetic anomalous effects. This is very clear in the case of sample B3, for which reflectivity curves on resonance (708.2 eV) and off-resonance (705 eV) are very similar (Fig. 6). In the case of sample B1, the strong increase in absorption at the edge explains the doubling of the periodicity for the Kiessig fringes. Off-resonance, the x rays penetrate deep enough to give interferences between both FePd layers, whereas on-resonance the x rays barely reach the deeper interface of the bottom FePd layer, so that the interference is mainly between both interfaces of the top FePd layer. The x rays reveal here the existence of a structural interface between both FePd layers, which is probably due to the segregation of Pd atoms to the surface, while heating the sample before the second layer is grown. Such an interface is not visible in the reflectivity from sample B3.

Rocking curves probe the lateral charge and magnetic order of the sample. Thus their magnetic periodicity (except for B4) gives rise to first-order magnetic satellites at either side of the specular peak.^{6,23} The satellite position gives the average magnetic periodicity and the satellite width gives the dispersion of the periodicity around its average value. The observed magnetic periodicities are given in Table III. They agree within 10% with the MFM results, which is a local measurement. The width of the satellites shows that this difference is within the dispersion of the magnetic periodicity.

We measured magnetic rod scans, i.e., at constant q_x , corresponding to the magnetic periodicity found with the transverse scans. Magnetic rod scans probe the periodic component of the magnetization. As can be seen from Fig. 7, the magnetic rod vanishes when the x rays are tuned off-resonance. Samples without spacers whose FePd layers all have the same thickness display Kiessig fringes corresponding to this thickness, whereas the other samples do not show oscillations. This can be explained by the weakness of the magnetic amplitude compared to the specular amplitude.

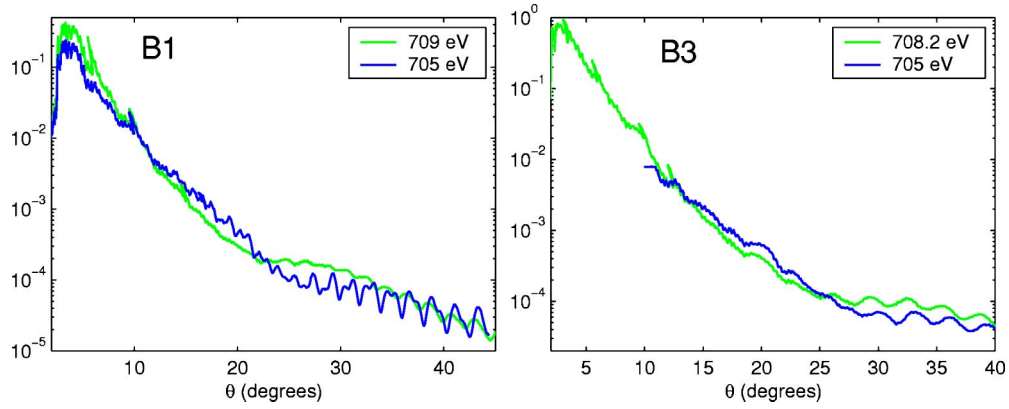


FIG. 6. (Color online) Soft x-ray reflectivity at the Fe L_3 absorption edge (light gray or green curve) and off-resonance (dark gray or blue curve) from the bilayers B1 (left) and B3 (right).

Strong interference effects, such as those obtained with periodic multilayers, are required to obtain measurable oscillations. The two samples with Pd spacers show strong oscillations because of the strong contrast between the magnetic density of the FePd layer and Pd spacer layer without Fe atoms.

Figure 7 also shows rod scans measured in the diffuse scattering of the specular peak ($q_x=0.02 \text{ nm}^{-1}$) and in the background of the transverse scan ($q_x=0.07 \text{ nm}^{-1}$). The long-period oscillation appearing in the diffuse scattering corresponds to the small thickness ($\sim 2 \text{ nm}$) of the protecting Pd coating, whose roughness is the main reason for the diffuse scattering around the specular peak. More precise quantitative information can be extracted from these magnetic rod scans, which requires the simulations that are presented in Sec. VI B.

V. MICROMAGNETIC MODELING

We will first outline the principle of the Gilbert-Landau-Lifshitz method³⁴ before presenting some results of the algorithm applied to the FePd thin-layer systems.

A. Principle of the GLFFT method

The principle of the simulation is based on dividing the magnetic volume into basis cells (nodes) that carry a local magnetic moment \mathbf{M}_i or, in reduced variables, $\mathbf{m}_i=\mathbf{M}_i/M_s$, and the minimization of the free energy calculated over the totality of these cells. The total energy can be written as

$$E_{\text{tot}} = E_{\text{ext}} + E_{\text{ex}} + E_{\text{ani}} + E_{\text{demag}}, \quad (3)$$

where E_{ext} is the Zeeman energy due to the external field, E_{ex} is the exchange energy, characterizing the ferromagnetism of the material (with exchange constant A_{ex}^i for layer i), E_{ani} is the anisotropy energy related to the constant K_u , and E_{demag} is the demagnetization energy connected to the shape of magnetic volume and the saturation magnetization M_s . In order to find an equilibrium magnetization distribution, the energy E_{tot} must be minimized by respecting two constraints: (1) the modulus of the magnetization vector is conserved and (2) the Brown condition at the interface of the two ferromag-

netic materials is respected, which reads as $A_{\text{ex}}^1 \partial \mathbf{m} / \partial \mathbf{n} = A_{\text{ex}}^2 \partial \mathbf{m} / \partial \mathbf{n}$, where \mathbf{n} is the normal direction. The latter expression reduces to $A_{\text{ex}} \partial \mathbf{m} / \partial \mathbf{n} = 0$ at the free surface of the sample.

The solution of the problem can be also carried out by applying the Gilbert-Landau-Lifshitz equation, which expresses the dynamic evolution of the local moment in the applied effective field

$$\frac{d\mathbf{m}}{dt} = -\gamma \mathbf{m} \times \mathbf{H}_{\text{eff}}, \quad (4)$$

where the effective field is given by $\mathbf{H}_{\text{eff}} = \mathbf{H} + \alpha(\mathbf{m} \times \mathbf{H})$, the coefficient γ is the gyromagnetic component and α is the Gilbert damping coefficient. The micromagnetic magnetic field \mathbf{H} is obtained by derivation of the free energy E_{tot} with respect to \mathbf{m} . To find the equilibrium state amounts to releasing the system according to the evolution equation [Eq. (4)]. This approach has the advantage that the criterion of canceling the exerted couple is more precise. Ideally, the minimizing process stops as the exerted torque vanishes. In practice,

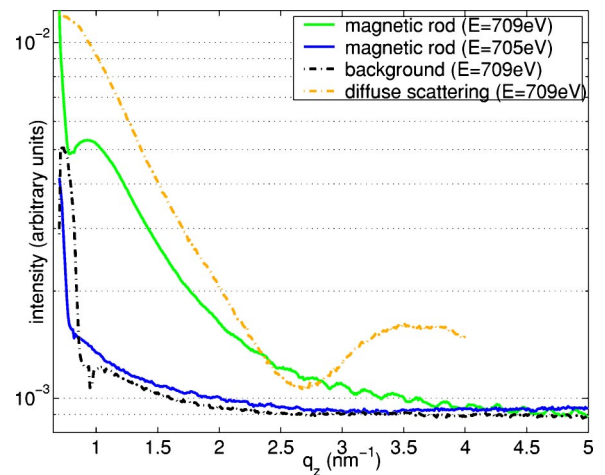


FIG. 7. (Color online) SXRMS rod scans (log scale) from the bilayer B1: magnetic rod scans on-resonance at 709 eV and off-resonance at 705 eV, diffuse ($q_x=0.02 \text{ nm}^{-1}$) and background with $q_x=0.07 \text{ nm}^{-1}$.

our approach assumes that the equilibrium configuration is achieved when the misalignment between the magnetization vector and the micromagnetic field is less than 10^{-6} .

The simulation algorithm, developed by Toussaint *et al.*,³⁵ consists of incrementing the variable of the time by a step δt and evaluating the magnetic configuration \mathbf{m}_i and the effective field $\mathbf{h}_i^{\text{eff}}$ on each node of the magnetic volume. The evolution of \mathbf{m}_i at each value of time t is then given by

$$\mathbf{m}_i(t + \delta t) = \mathbf{m}_i(t) \cos(h_i^{\text{eff}} \delta t) + \frac{\sin(h_i^{\text{eff}} \delta t)}{h_i^{\text{eff}}} [\mathbf{h}_i^{\text{eff}} \times \mathbf{m}_i(t)]. \quad (5)$$

The time step δt is chosen smaller than the critical time step to observe convergence and stability during the numerical integration of the Gilbert-Landau-Lifshitz equations. This condition ensures that the magnetization distribution is locally quasiparallel to the effective magnetic field lines. In this sense, the algorithm leads well to a local minimum of the micromagnetic energy while respecting the normalization constraint of the vector magnetization.

Finally, the calculation of the effective magnetic field is considerably accelerated using the fast Fourier transform (FFT) technique that allows one to reduce a convolution operation in real space to a simple multiplication in reciprocal space, hence the name ‘‘GL_{FFT} method.’’^{35,36}

B. Modeling results

Micromagnetic simulations were carried out with the aim to obtain the three-dimensional magnetization profiles in the FePd layers. The parameters were chosen as follows: the exchange length $l_{\text{ex}} = 3.2$ nm, the exchange constant $A_{\text{ex}} = 6.8 \times 10^{-7}$ erg/cm; for the magnetic anisotropy we take the typical values, $Q=0$ and 1.8, describing the soft and the strong anisotropy layers, respectively.

The representative magnetic volume corresponds to a section of the film whose width is equal to the stripe period p_{mag} and whose height is equal to the film thickness e (typically 20–60 nm for bilayers and trilayers). The system is assumed to be invariant along the y direction, i.e., parallel to the stripes, and therefore depends only on the x and z dimensions. The division in cells was carried out using a grid of 128×64 magnetic nodes. The size of these magnetic cells is ~ 1 nm, which corresponds typically to an in-plane density of 10 Fe atoms per cell. The results obtained for the bilayers and trilayers are presented in Fig. 8. The presentation of the three-dimensional magnetization profiles is accomplished in the xz plane with vectors to indicate the m_x and m_z components and with color to describe the third component m_y [gradually increasing from light gray (green in web version) to dark gray (red in web version)]. Simulations for monolayers, which can be found in Ref. 25, show that for fixed thickness the magnetic period increases with increasing anisotropy. For the bilayers and trilayers, this is less obvious to conclude, since the magnetic period not only depends on the total thickness but also on the individual layer thicknesses. The periods resulting from the simulations are roughly comparable with the ones imaged by MFM and measured by

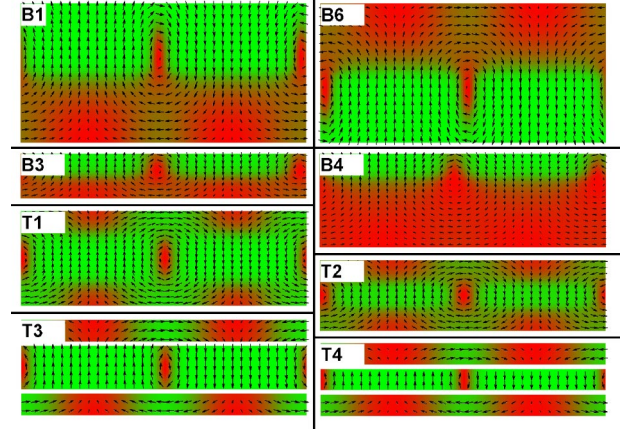


FIG. 8. (Color online) Micromagnetic GL_{FFT} simulations for the bilayers B1, B3, B4, and B6 and the trilayers T1, T2, T3, T4 with $Q=0$ for the disordered layers and $Q=1.8$ for the ordered layers. It is noticed that the result of simulation for B6 corresponds to that of B1 turned by 180° . Each cell (~ 1 nm containing ~ 10 Fe atoms) is represented by a normalized magnetization vector, shown in the m_x and m_z direction while the third component m_y is represented by the color [gradually increasing from light gray (green in web version) to dark gray (red in web version)].

SXRMS, and the evolution from one sample to the next shows the same trend.

For the bilayer B4, the simulation leads to the formation of alternating up and down domains, whereas neither the SXRMS nor the MFM measurements showed evidence for a magnetic periodicity. This suggests that the simulations describe the system in the ideal situation. The particular deposition conditions and the presence of defects can considerably deteriorate the theoretically expected magnetization profile.

VI. NUMERICAL SIMULATION OF SXRMS

A. Theoretical description of the method

In the following numerical simulations for the SXRMS, the reflection and transmission through interfaces will be treated in an optical way, but the magnetic scattering occurring in the FePd layers will be based only on the kinematical model.

The first step in the simulation is the calculation of the wave vectors of the incident and outgoing waves in the different layers of the sample. The normal component k_i^z of the wave vector in layer i (where 0 stands for the vacuum, 1 for the Pd capping layer, and 2 for the FePd layers considered as one) is obtained as

$$k_i^z = k_0 \sqrt{\left(\frac{k_0^z}{k_0}\right)^2 - 2\delta_i - 2i\beta_i}, \quad (6)$$

where δ_i and β_i are the optical constants of the layer i without the magnetic part, and k_0 is the modulus wave vector in vacuum. We define $\mathbf{q} = \mathbf{k}_2^{\text{out}} - \mathbf{k}_2^{\text{in}}$ as the scattering vector in the FePd layers. Since $\beta_i \neq 0$ in the sample, k_i^z and \mathbf{q} have an imaginary part related to the absorption. The absorption

length in FePd, defined as the length where the beam intensity is reduced by e^{-1} , is directly related to the optical parameters in FePd, which vary strongly across the Fe L_3 edge. Therefore the photon energy is one of the most important parameters.

The second step in the simulation is the calculation of the transmission coefficients T_{in} and T_{out} through the capping layer, representing the effects on both incident and outgoing amplitudes, at the vacuum–capping layer interface and at the capping layer–magnetic layer interface. T_{in} is calculated as

$$T_{\text{in}} = \frac{t_{01}t_{12} \exp(ik_1^z e_1)}{1 + r_{10}r_{12} \exp(2ik_1^z e_1)}, \quad (7)$$

where

$$t_{ij} = \frac{2k_i^z}{k_i^z + k_j^z}, \quad (8)$$

$$r_{ij} = \frac{k_i^z - k_j^z}{k_i^z + k_j^z} \quad (9)$$

are the Fresnel coefficients for transmission and reflection, respectively. T_{out} is calculated in the same way.

The third step in the simulation is the calculation of the diffraction process in the magnetic layers, starting from the micromagnetic modeling results and stretching over three stages, corresponding to the three different spatial scales, namely atomic, nanoscopic, and micromagnetic.

(1) The *atomic scale* determines the scattering factors of the Fe and Pd atoms. While the scattering factor of the Pd atoms can be directly obtained from the international data tables and has no magnetic part since the x-ray energy is far from any Pd edge, the scattering factor of the Fe atoms is given in good approximation by^{32,33}

$$f_{\text{Fe}} = F_0(\mathbf{e}'^* \cdot \mathbf{e}) - iF_1(\mathbf{e}'^* \times \mathbf{e}) \cdot \mathbf{m}, \quad (10)$$

where \mathbf{e} and \mathbf{e}' are the polarization directions of the incident and scattered beam, respectively, and \mathbf{m} is the magnetic moment of the Fe atom obtained from the micromagnetic simulation (where we assume that it is homogenous over a micromagnetic cell). The scattering amplitudes F_0 and F_1 vary strongly across the L_3 edge, so that the precise choice of the photon energy is important to reproduce the experimental curves. With the incident polarization perpendicular to the scattering plane (i.e., σ polarization), Eq. (10) reduces to

$$f_{\text{Fe}} = F_0 - iF_1 \mathbf{k}_2^{\text{out}} \cdot \mathbf{m}. \quad (11)$$

(2) The *nanometric scale* determines the scattering factors f_{jk} of each cell (~ 1 nm) of the micromagnetic simulation. Assuming that the crystallographic structure and the magnetic moment of the Fe atoms are uniform over each micromagnetic cell, we only need to determine a nanoscopic structure factor S_{jk} of the cell by summing the scattering amplitudes over the atoms of the micromagnetic cell (j, k). This is achieved in two steps, first by summing the scattering amplitudes over the atoms of the crystallographic cell, then by summing the resulting amplitudes over the crystallographic cells of the micromagnetic cell. In the disordered fcc

structure (with a quasi-isotropic distribution of Fe and Pd atoms) the average scattering factor is used, while in the ordered $L1_0$ structure the Fe and Pd planes are alternating. We obtain three reference values: one for the fcc structure and two for the $L1_0$ structure, because the charge and magnetic amplitudes have different distributions in the latter case. Thus we have to decompose S_{jk} into its charge and magnetic parts, S_{jk}^{ch} and S_{jk}^{mag} , respectively. The scattering factor f_{jk} of the cell (j, k) can then be written as

$$f_{jk} = F_0(\mathbf{e}'^* \cdot \mathbf{e})S_{jk}^{\text{ch}} - iF_1(\mathbf{e}'^* \times \mathbf{e}) \cdot \mathbf{m}_{jk}S_{jk}^{\text{mag}}. \quad (12)$$

(3) For the *micromagnetic scale* we need to sum the contributions of the different cells (with index j, k) over the entire volume of the micromagnetic simulation, in order to arrive at the scale of the magnetic period (~ 100 nm),

$$F(\mathbf{q}) = \sum_{jk} f_{jk} e^{i\mathbf{q} \cdot \mathbf{r}_{jk}}. \quad (13)$$

In the case of transverse scans, the broadening of the magnetic satellites can be well-reproduced using a Lorentzian function $L_{\text{mag}}(q_x)$. This broadening takes into account the variation of the magnetic period over the illuminated area. The width of the Lorentzian function is $2\pi/l_{\text{mag}}$, where l_{mag} is the correlation length of the magnetic periodicity. Likewise, the broadening of the specular peak is given by a Lorentzian function $L_{\text{ch}}(q_x)$. However, no practical information could be extracted from its width due to the low number of experimental points describing the peak shape.

The total scattering amplitude F_{tot} , which can be decomposed into a charge term $F_{\text{tot}}^{\text{ch}}$ and a magnetic term $F_{\text{tot}}^{\text{mag}}$, is then expressed by the convolution of the line shape functions with the summation over the volume of the micromagnetic simulation,

$$\begin{aligned} F_{\text{tot}}(\mathbf{q}) &= F_{\text{tot}}^{\text{ch}} + F_{\text{tot}}^{\text{mag}} \\ &= F_0(\mathbf{e}'^* \cdot \mathbf{e}) \left(\sum_{jk} S_{jk}^{\text{ch}} e^{i\mathbf{q} \cdot \mathbf{r}_{jk}} \right) L_{\text{ch}}(q_x) \\ &\quad - iF_1(\mathbf{e}'^* \times \mathbf{e}) \cdot \left(\sum_{jk} \mathbf{m}_{jk} S_{jk}^{\text{mag}} e^{i\mathbf{q} \cdot \mathbf{r}_{jk}} \right) L_{\text{mag}}(q_x). \end{aligned} \quad (14)$$

Finally, the theoretical intensity is obtained as

$$I_{\text{th}} = |F_{\text{tot}}(\mathbf{q})|^2. \quad (15)$$

It is also necessary to include the experimental background noise (constant I_0), a correction for the illuminated sample area ($\sin^{-1} \theta$), the vertical roughness σ (for specular and magnetic rod scans) occurring in the Debye-Waller factor $R_z(q_z) = \exp(-\sigma^2 q_z^2)$, and the diffuse background modeled by a Gaussian $I_d(q_x)$ connected to a lateral roughness ξ_h (for transverse scans). The calculated intensity is then for transverse scans,

$$I = I_0 + |T_{\text{in}}|^2 |T_{\text{out}}|^2 (I_d + CI_{\text{th}}) \sin^{-1} \theta, \quad (16)$$

and for the magnetic rod scans,

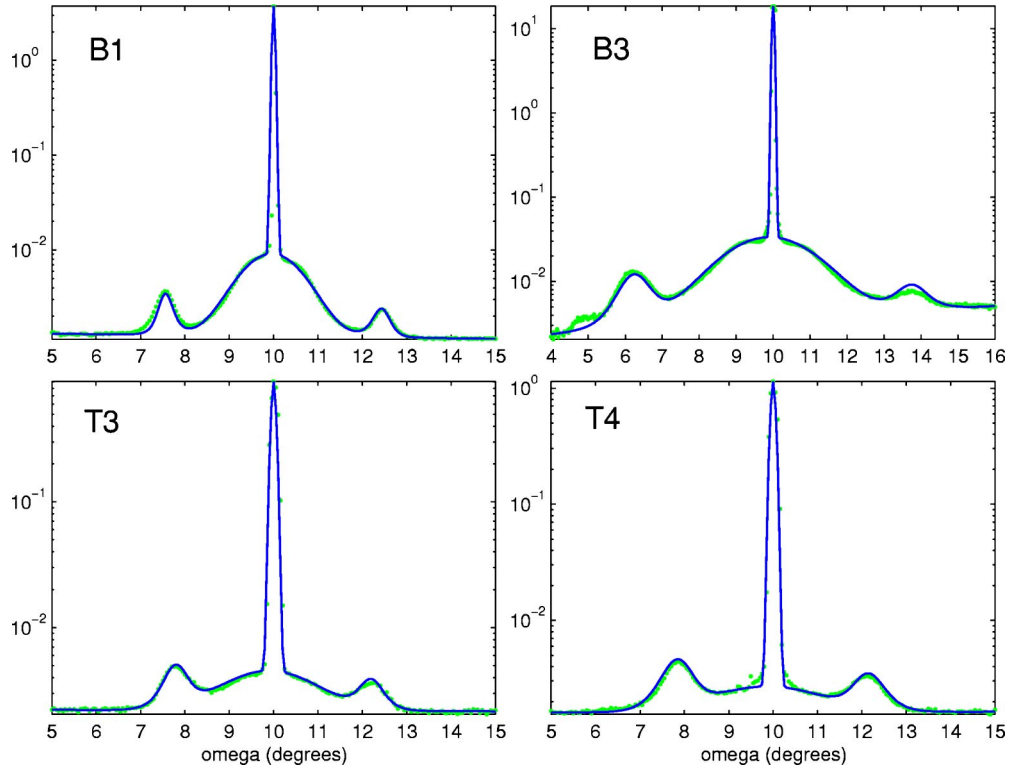


FIG. 9. (Color online) SXRMS transverse scans and their numerical simulations using the calculated micromagnetic configurations. Experimental curves (green/gray filled dots) and simulated curves (blue/black line).

$$I = I_0 + C|T_{\text{in}}|^2|T_{\text{out}}|^2 R_z I_{\text{th}} \sin^{-1} \theta, \quad (17)$$

where C in both cases is an experimental multiplication factor.

B. SXRMS simulation results

Simulations were carried out for transverse scans (Fig. 9) and magnetic rod scans (Fig. 10) on the bilayers B1 and B3 and the trilayers T3 and T4, starting from the micromagnetic simulations containing 128 nodes along x and 32 or 64 along z . The dimensions p_{mag} and e_{mag} , initially imposed by the micromagnetic simulation, were readjusted in order to give a better agreement with the SXRMS measurements. If such a readjustment proves to be necessary, it reveals that certain intrinsic parameters used for the micromagnetic calculations (such as the anisotropy Q or the exchange length l_{ex}) also require readjustment in order to find an agreement with the SXRMS measurements.

The simulated results agree remarkably well with the measured results, which makes it possible to determine various parameters, whose values are collected in Table III.

The transverse scans give the values of the average magnetic stripe period p_{mag} and the magnetic correlation length l_{mag} (5–50 stripes, depending on the sample) directly from the magnetic satellite positions and widths. The average magnetic periodicity can be obtained within an accuracy of 1 nm. The asymmetry ratio of the two magnetic peaks at either side of the specular peak in the rocking curves in Fig. 9 is related to the in-plane and perpendicular component of the magnetization, as has been described in Ref. 26. It leads

to the degree of perpendicular anisotropy and the closure domain size. While p_{mag} and l_{mag} can be estimated without any simulation, the asymmetry ratio requires a simulation using the model presented in Sec. VI A. From the width of the diffuse scattering around the specular peak, we obtain the lateral roughness ξ_h .

TABLE III. Parameters obtained from the numerical simulation for the bilayers B1 and B3 and trilayers T3 and T4. From the transverse scan, the magnetic period p_{mag} , magnetic correlation length l_{mag} , and lateral roughness ξ_h (diffuse background). From the magnetic rod at the indicated photon energy of the calculation, the corresponding absorption length l_{abs} , magnetic layer thickness e_{mag} (including spacers), the coating layer thickness e_{coating} , and the vertical roughness σ .

Sample	B1	B3	T3	T4
Simulation energy (eV)	708	706.2	707.9	707.7
l_{abs} (nm)	33	47	32	30
Transverse scans (Fig. 9)				
p_{mag} (nm)	118	76	132	137
l_{mag} (nm)	420	200	300	230
ξ_h (nm)	71	40	47	40
Magnetic rods (Fig. 10)				
e_{mag} (nm)	58.0	19.4	43.7	32.4
e_{coating} (nm)	2.0	0.8	3.1	3.4
σ (nm)	0.28	0.33	0.48	0.39

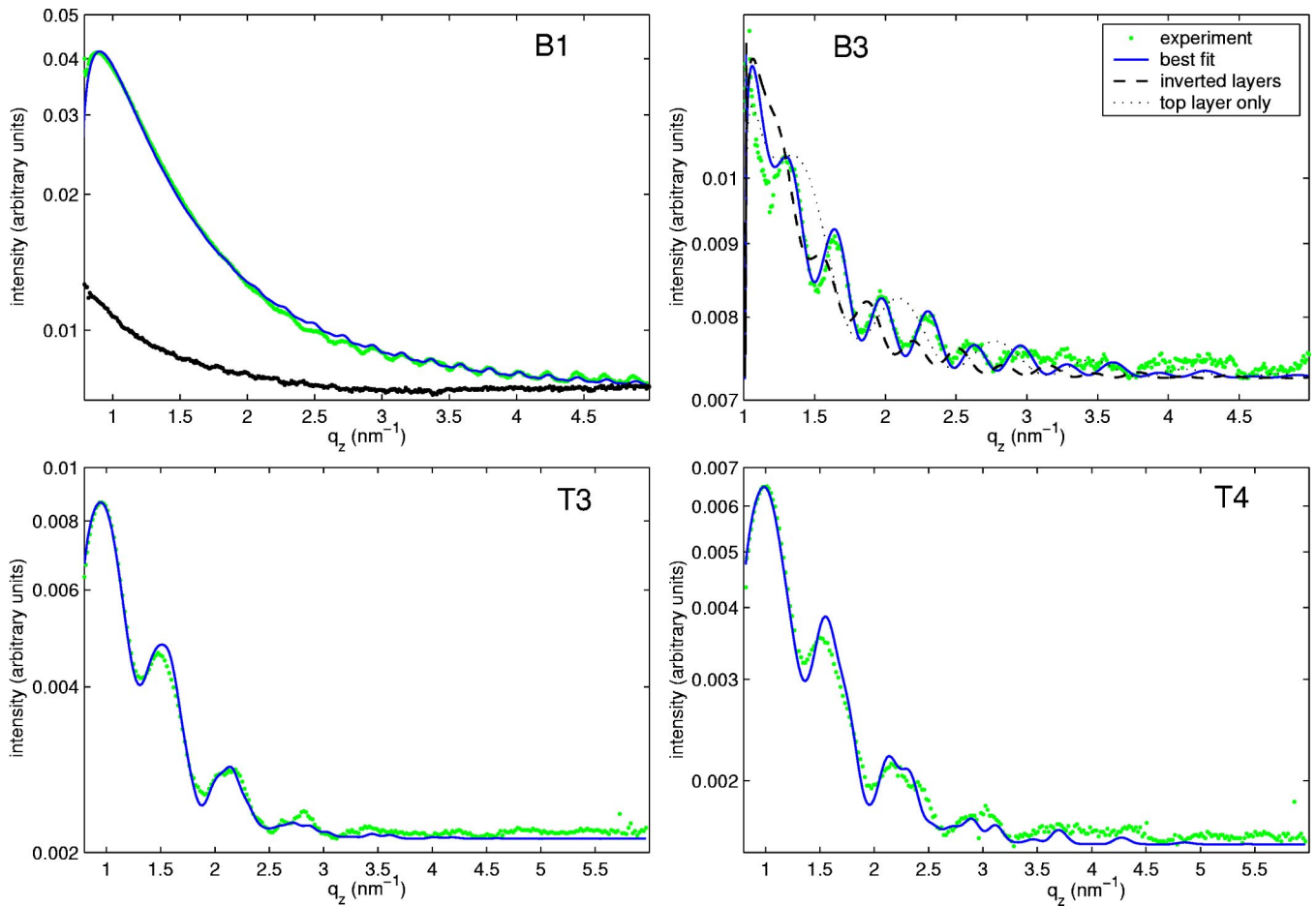


FIG. 10. (Color online) SXRMS magnetic rods and their numerical simulations using the calculated micromagnetic configurations. Experimental curves (green/gray filled dots) and simulated curves (blue/black line). For sample B3 (top right), two others simulations are performed: one with the FePd in reverse order (black dashed curve) and one with the magnetization of the bottom layer set to zero (black dots).

From the magnetic rod scans, we can determine the total magnetic thickness, including the two, or three, FePd layers and their spacer layers. For soft x rays the reflectivity measurements are accurate to 1 Å. In the case of sample B1, the main fringes observed in the magnetic rod scan are primarily due to the interference in the FePd top layer only, because the absorption is such that the x rays barely penetrate the FePd bottom layer. The thickness of the Pd coating can also be determined, but being only 2 to 3 nm thick, it just gives a single large oscillation in the specular and magnetic rod scans. It is therefore difficult to evaluate within good accuracy, unless the sample is very well aligned in the diffractometer. This was probably the case for sample B1, but certainly not for sample B3. We used a single roughness parameter to reproduce the decrease in the curves. This parameter includes the roughness at the layer interfaces, but above all it is dominated by the surface roughness. We know from reflection high energy electron diffraction (RHEED) measurements during the deposition that the interfaces have a very small roughness (less than one atomic layer) and their effect is reduced by the absorption of the x rays in the sample. A more sophisticated model with different roughnesses was developed, but the results did not give a signifi-

cantly better improvement. The choice of the photon energy, determining the absorption length, is crucial: it must be adjusted within 0.1 eV. Since the photon energy of the beamline was drifting slowly with time we do not know the absolute experimental energies within 1 eV and we only give the energies for the simulations in Table III.

Finally, the good agreement between measured and calculated magnetic rod scans confirms the vertical magnetic profile calculated by the micromagnetic simulations. In Fig. 10, three different simulations are presented for sample B3: one from the calculated magnetic configuration, another one from the same structure with both FePd layers in reverse order, and the last one from a structure where the magnetization in the bottom layer has been set to zero. The huge difference between the three simulated magnetic rods shows the sensitivity of the technique to the magnetic configuration, which in this case cannot be probed by specular measurements.

The information that can be obtained from the SXRMS measurements on this type of system can be summarized as follows. (i) Transverse scans give the average magnetic stripe period p_{mag} and the magnetic correlation length l_{mag} directly from the magnetic satellite positions and the widths,

as well as the lateral roughness ξ_h from the width of the diffuse scattering around the specular peak. The intensity ratio of the magnetic satellites leads to the closure domain size. (ii) The reflectivity measurements at the Fe L_3 resonance give the in-depth profile of the zeroth-order coefficient of the lateral Fourier transform (i.e., the laterally constant part) of the magnetization. In our case, the only component with a zeroth-order contribution, which is parallel to the stripes, is not probed in this geometry. (iii) The magnetic rod scans give the in-depth profile of the first-order coefficient of the magnetization. This measurement is complementary to reflectivity measurements for laterally periodic systems.

VII. SUMMARY AND CONCLUSIONS

Epitaxially grown thin films of FePd alloy form self-organizing magnetic patterns with periodic structures. By using layers of different magnetic anisotropy in bilayers or trilayers of FePd alloys it is possible to change the magnetic interaction and the stripe pattern, which is of great scientific and technological interest because it allows one to tailor the properties of these self-organizing magnetic systems.

Magnetic domain patterns of FePd samples were measured by imaging the magnetic stray lines using MFM, while the global magnetic anisotropy of the samples was obtained from VSM performed in both parallel and perpendicular geometry. The perpendicular magnetic anisotropy can be quantified by the quality factor Q which depends on both the thicknesses and the growth conditions of the layers. The average values of the quality factor obtained by VSM were compared with theoretical values of the average anisotropy weighted by the film thicknesses. The measured average values are shown to be in relatively good agreement with the theoretical values. SXRMS at resonance shows a strong sensitivity to the different magnetization components and the periodicity of the profile in the layers. Measurement of magnetic rod scans, which can be compared with the reflectivity rod scans, makes it possible to obtain the in-depth magnetic profile.

The FePd bi- and trilayers were numerically modeled with micromagnetic simulations using the Gilbert-Landau-Lifshitz method with the aim to obtain the three-dimensional

magnetization profiles within the various layers. The simulated stripe periods are roughly comparable with the stripe periods measured by MFM and SXRMS. For some particular depositions conditions no stripe pattern was observed, although it was predicted for ideal samples without defects.

The simulation of the diffraction process in the magnetic layers was performed, starting from the micromagnetic modeling results, stretching over three stages, corresponding to the three different spatial scales, namely atomic, nanoscopic, and micromagnetic. The dimensions of the magnetic stripe period and layer thickness, initially imposed by the micromagnetic simulation, were iterated to give a better agreement with the SXRMS measurements. These numerical simulations were carried out for both transverse scans and magnetic rod scans. The positions and widths of the magnetic satellites in the transverse scan give directly the values of the average magnetic stripe period and the magnetic correlation length. The asymmetry ratio of the magnetic peaks around the specular reflection in the rocking curve gives, with the use of simulations, the degree of perpendicular anisotropy and the closure-domain size. The width of the diffuse scattering around the specular peak gives the lateral roughness.

The good agreement between the micromagnetic modeling simulations and the experimental SXRMS results demonstrate that SXRMS provides in-depth information that cannot be obtained from either MFM or VSM. Thus using the results of micromagnetic modeling, numerical simulation of the SXRMS makes it possible to account for the magnetic profile and its evolution within the film. Such numerical simulations allow modeling of the experimental reflectivity and magnetic rod scans in order to verify a variety of quantities, such as the absorption length at resonance, layer thicknesses, structural roughness, average magnetic stripe period, magnetic correlation length, and the presence of magnetic interfaces.

ACKNOWLEDGMENTS

We would like to thank M. D. Roper and I. W. Kirkman for beamline support at Daresbury, J.-P. Attané and Y. Samson for MFM measurements, and J. M. Tonnerre for providing atomic scattering factor files.

¹V. Gehanno, A. Marty, B. Gilles, and Y. Samson, *Phys. Rev. B* **55**, 12552 (1997).

²G. van der Laan, B. T. Thole, G. A. Sawatzky, J. B. Goedkoop, J. C. Fuggle, J. M. Esteva, R. Karnatak, J. P. Remeika, and H. A. Dabkowska, *Phys. Rev. B* **34**, 6529 (1986).

³B. T. Thole, P. Carra, F. Sette, and G. van der Laan, *Phys. Rev. Lett.* **68**, 1943 (1992).

⁴H. A. Dürr, G. Y. Guo, G. van der Laan, J. Lee, G. Lauhoff, and J. A. C. Bland, *Science* **277**, 213 (1997).

⁵G. van der Laan, H. A. Dürr, E. Dudzik, M. D. Roper, S. P. Collins, T. P. A. Hase, and I. Pape, *Synchrotron Radiat. News* **12**, 5 (1999).

⁶G. van der Laan, *Synchrotron Radiat. News* **14**, 32 (2001).

⁷G. van der Laan and B. T. Thole, *Phys. Rev. B* **43**, 13401 (1991).

⁸H. A. Dürr, E. Dudzik, S. S. Dhesi, J. B. Goedkoop, G. van der Laan, M. Belakhovsky, C. Mocuta, A. Marty, and Y. Samson, *Science* **284**, 2166 (1999).

⁹J.-M. Tonnerre, in *Magnetism and Synchrotron Radiation*, edited by E. Beaurepaire, B. Carrière, and J.-P. Kappler (Les Éditions de Physique, Les Ulis, 1996), p. 245.

¹⁰T. P. A. Hase, I. Pape, B. K. Tanner, H. Dürr, E. Dudzik, G. van der Laan, C. H. Marrows, and B. J. Hickey, *Phys. Rev. B* **61**, R3792 (2000).

¹¹J. F. MacKay, C. Teichert, D. E. Savage, and M. G. Lagally, *Phys. Rev. Lett.* **77**, 3925 (1996).

¹²J. F. MacKay, C. Teichert, and M. G. Lagally, *J. Appl. Phys.* **81**,

- 4353 (1997).
- ¹³R. M. Osgood, S. K. Sinha, J. W. Freeland, Y. U. Idzerda, and S. D. Bader, *J. Appl. Phys.* **85**, 4619 (1999).
- ¹⁴J. B. Kortright and S. K. Kim, *Phys. Rev. B* **62**, 12216 (2000).
- ¹⁵J. B. Kortright, S. K. Kim, G. P. Denbeaux, G. Zeltzer, K. Takano, and E. E. Fullerton, *Phys. Rev. B* **64**, 092401 (2001).
- ¹⁶A. Mirone, M. Sacchi, E. Dudzik, H. A. Dürr, G. van der Laan, A. Vaurès, and F. Petroff, *J. Magn. Magn. Mater.* **218**, 137 (2000).
- ¹⁷N. Jaouen, J.-M. Tonnerre, D. Raoux, E. Bontempi, L. Ortega, M. Muenzenberg, W. Felsch, A. Rogalev, H. A. Dürr, E. Dudzik, G. van der Laan, H. Maruyama, and M. Suzuki, *Phys. Rev. B* **66**, 134420 (2002).
- ¹⁸K. Chesnel, M. Belakhovsky, F. Livet, S. P. Collins, G. van der Laan, S. S. Dhesi, J. P. Attané, and A. Marty, *Phys. Rev. B* **66**, 172404 (2002).
- ¹⁹N. Jaouen, G. van der Laan, T. K. Johal, F. Wilhelm, A. Rogalev, S. Mylonas, and L. Ortega, *Phys. Rev. B* **70**, 094417 (2004).
- ²⁰K. Chesnel, M. Belakhovsky, G. van der Laan, F. Livet, A. Marty, G. Beutier, S. P. Collins, and A. Haznar, *Phys. Rev. B* **70**, 180402(R) (2004).
- ²¹K. Chesnel, M. Belakhovsky, A. Marty, G. Beutier, G. van der Laan, and S. P. Collins, *Physica B* **345**, 148 (2004).
- ²²P. Kamp, A. Marty, B. Gilles, R. Hoffmann, S. Marchesini, M. Belakhovsky, C. Boeglin, H. A. Dürr, S. S. Dhesi, G. van der Laan, and A. Rogalev, *Phys. Rev. B* **59**, 1105 (1999).
- ²³E. Dudzik, S. S. Dhesi, H. A. Dürr, S. P. Collins, M. D. Roper, G. van der Laan, K. Chesnel, M. Belakhovsky, A. Marty, and Y. Samson, *Phys. Rev. B* **62**, 5779 (2000).
- ²⁴E. Dudzik, S. S. Dhesi, S. P. Collins, H. A. Dürr, G. van der Laan, K. Chesnel, M. Belakhovsky, A. Marty, Y. Samson, and J. B. Goedkoop, *J. Appl. Phys.* **87**, 5469 (2000).
- ²⁵G. van der Laan, K. Chesnel, M. Belakhovsky, A. Marty, F. Livet, S. P. Collins, E. Dudzik, A. Haznar, and J. P. Attané, *Superlattices Microstruct.* **34**, 107 (2003).
- ²⁶G. Beutier, A. Marty, K. Chesnel, M. Belakhovsky, J. C. Tousseint, B. Gilles, G. van der Laan, S. P. Collins, and E. Dudzik, *Physica B* **345**, 143 (2004).
- ²⁷A. Hubert and R. Schaeffer, *Magnetic Domains: The Analysis of Magnetic Microstructures* (Springer-Verlag, Berlin, 1998).
- ²⁸Y. Samson, A. Marty, R. Hoffmann, V. Gehanno, and B. Gilles, *J. Appl. Phys.* **85**, 4604 (1999).
- ²⁹B. Kaplan and G. Gehring, *J. Magn. Magn. Mater.* **128**, 111 (1993).
- ³⁰V. Gehanno, Y. Samson, A. Marty, B. Gilles, and A. Chamberod, *J. Magn. Magn. Mater.* **172**, 26 (1997).
- ³¹M. D. Roper, G. van der Laan, H. A. Dürr, E. Dudzik, S. P. Collins, M. C. Miller, and S. P. Thompson, *Nucl. Instrum. Methods Phys. Res. A* **467-468**, 1101 (2001).
- ³²J. P. Hannon, G. T. Trammell, M. Blume, and D. Gibbs, *Phys. Rev. Lett.* **61**, 1245 (1988).
- ³³G. van der Laan, E. Dudzik, S. P. Collins, S. S. Dhesi, H. A. Dürr, M. Belakhovsky, K. Chesnel, A. Marty, Y. Samson, and B. Gilles, *Physica B* **283**, 171 (2000).
- ³⁴M. Schabes and H. Bertman, *J. Appl. Phys.* **64**, 1347 (1988).
- ³⁵J. Toussaint, A. Marty, N. Vukadinovic, J. Youssef, and M. Labruno, *Comput. Mater. Sci.* **24**, 175 (2002).
- ³⁶D. Berkov, K. Ramstöck, and A. Hubert, *Phys. Status Solidi A* **137**, 207 (1993).